Composition of Coronal Hole Boundary Layers at Low Heliographic Latitudes

K. Delano[1,2], H. A. Elliott[2,1], S. T. Lepri[3], S. A. Fuselier[2,1]

[1]University of Texas at San Antonio, San Antonio, TX, USA
[2]Southwest Research Institute, San Antonio, TX, USA
[3]University of Michigan, Ann Arbor, MI, USA

Corresponding Author: Kevin Delano (kevin.delano@utsa.edu)

Key Points

- ACE composition measurements indicate that the largest coronal hole extension of 2003 has a thick CHBL distinct from its core
- A CHBL is also observed in a small, inward-polarity coronal hole in 2003; its speed range is not as broad as that of the largest extension

This is the author manuscript accepted for publication and has undergone full peer review but has not been through the copyediting, typesetting, pagination and proofreading process, which may lead to differences between this version and the Version of Record. Please cite this article as doi: 10.1029/2021JA029187.

Abstract

In some polar coronal holes, previous studies have identified a coronal hole boundary layer (CHBL) which is different in composition from the coronal hole core region. However, compositionally distinct CHBL structure at low heliographic latitudes remains underexplored. Using solar wind composition measurements from the Advanced Composition Explorer (ACE), we study two particular low-latitude coronal holes of 2003: a large polar hole extension with outward magnetic polarity and a smaller equatorial hole with inward magnetic polarity. For both of these coronal holes, we examine the distribution of two composition parameters, the O^{7+} to O^{6+} charge state density ratio ($n(O^{7+})/n(O^{6+})$) and the Fe to O abundance ratio (n(Fe)/n(O)), and find that each hole has an identifiable CHBL based on an anticorrelation of solar wind speed and $n(O^{7+})/n(O^{6+})$. We also examine the FIP (first ionization potential) effect in the CHBL using n(Fe)/n(O) and find that there is no significant change from the CHBL to the core region for one of the coronal holes we study, while the other coronal hole has a noticeable decrease in n(Fe)/n(O) values in its core. Finally, we discuss our results in the context of previous work studying CHBL structure.

1. Introduction

The solar wind is typically separated into two categories: slow solar wind, with average velocities of less than 450 km/s, and fast solar wind, with average velocities greater than 500 km/s (e.g. Cranmer, 2002, Zurbuchen, 2007). Slow wind and fast wind also have differences in heavy ion composition, reflecting different sources at the Sun. Relative to fast wind, slow wind is enhanced in ions with high charge states as well as

elements with a low first ionization potential (e.g. Meyer, 1985, Geiss et al., 1995). The source of slow wind is an actively debated topic and not the focus of this paper. Fast wind generation has long been accepted to be from coronal holes (e.g. Hundhausen, 1977, Hollweg and Isenberg, 2002, Zurbuchen, 2007), which are regions of the Sun's corona characterized by open magnetic field lines and lower temperatures than the rest of the corona (Zirker, 1977, Landi, 2008). Since coronal holes are cooler and less dense than the surrounding coronal plasma, the low-energy environment makes it unlikely for high charge states to form (Owocki et al., 1983, Laming and Lepri, 2007). These conditions result in reduced ionization of solar wind plasma, evident in certain observed ion charge state ratios—$n(O^{7+})/n(O^{6+})$, for example—compared to slow wind (Geiss et al., 1995, von Steiger et al., 2000, Zhao et al., 2009). Additionally, abundances of low-FIP ions in fast wind are similar to those of the photosphere (Meyer, 1985, von Steiger et al., 1992, von Steiger et al., 2000) and chromosphere (Geiss et al., 1995) while slow wind tends to have enhanced abundances of low-FIP ions similar to levels found in large coronal loops. This enhancement in low-FIP ions in slow wind is commonly referred to as the FIP effect and is mostly absent in fast wind (Laming, 2015). Open magnetic field lines emanating from coronal holes have either outward polarity (pointing away from the Sun) or inward polarity (pointing toward the Sun). In both cases, fast wind streams that propagate outward into interplanetary space remain magnetically connected to the Sun. The Sun's largest coronal holes are found at its poles, but smaller coronal holes appear at all heliographic latitudes. Although low-latitude coronal holes are not as long-lived as polar coronal holes, they tend to last several solar rotations (Zirker, 1977, Krista et al., 2018).

Observational studies of the plasma parameters and ion composition of polar high speed streams (e.g. McComas et al., 1998b, McComas et al., 2002, McComas et al., 2003) have shown that coronal holes have a boundary layer which is distinct from the core of the hole. McComas et al. (1998b) observed a gradual increase in solar wind speed (rather than a sharp transition) when Ulysses passed from the slow wind into a fast stream from a polar coronal hole, indicating that some coronal holes have a thick boundary region. This region, known as the coronal hole boundary layer (CHBL), likely exists near the interface of open field lines and closed loops, as shown by the cartoon in Figure 1. McComas et al. (2002) further examined boundary regions of coronal holes using nine fast solar wind streams from polar coronal holes between 2000 and 2001. They showed that oxygen and carbon freezing-in temperatures tended to steadily increase as proton speed decreased during rarefactions immediately following high-speed streams. This gradual, monotonic anticorrelation of solar wind speed and freezing-in temperatures is a distinguishing compositional signature of a CHBL (Schwadron et al., 2005).

Although CHBL structure has been separately observed in coronal holes at low heliographic latitudes (Foullon et al., 2011, Stakhiv et al., 2016, Zhao et al., 2017) and high heliographic latitudes with Ulysses (e.g. McComas et al., 1998b, McComas et al., 2002), no comparisons have been made between the CHBLs of polar hole extensions and equatorial holes. Elliott et al. (2012) presented observations which suggest that such a comparison is possible with the low-latitude coronal holes of 2003. Using proton temperature and proton speed measurements from the Advanced Composition Explorer (ACE) spacecraft, Elliott et al. (2012) plotted the Temperature-Velocity (T-V) distribution of the solar wind (excluding CMEs) in 2003 and sorted the T-V distribution

by magnetic polarity. Noticing a distinct group of data points with outward polarity, they isolated this high-speed population by drawing a box around it (referred to as the T-V box in this work), as shown in Figure 2b. This box had left and right boundaries of 570 km/s and 830 km/s and upper and lower boundaries based on a linear fit to the outward polarity high-speed data. Although the fit is linear, the plot is in semi-log format in order to accommodate the smaller range of speeds in comparison to the larger range of temperatures for the dataset. By visually matching the coronal hole maps shown in Figure 3 (originally published in Elliott et al. (2010)) to the high-speed peaks with the corresponding polarity in the time series plot in Figure 2d, Elliott et al. (2012) concluded that the points in the T-V box with outward polarity come from a large, long-lasting polar extension with outward polarity. Additionally, as shown in Figure 2c, there are a number of points with inward polarity that lie within the T-V box as well, and these correspond to a smaller, inward-polarity coronal hole with no connections to either of the Sun's poles. As suggested by the plot of solar wind speed versus time for observations in 2003 (Figure 2d), the fast wind emitted by this smaller hole with inward polarity has similar properties to the high-speed streams of the large polar extension. Thus, both the larger outward-polarity hole (which we refer to as CH-A in this work) and the smaller inward-polarity hole (which we refer to as CH-B) are likely candidates to have a defined CHBL and core region.

In this work, we use solar wind composition measurements from ACE and the T-V box defined in Elliott et al. (2012) in conjunction with coronal hole maps from Elliott et al. (2010) to determine whether or not the two aforementioned low-latitude coronal holes of 2003 have an identifiable CHBL. By examining the distribution of two

composition parameters, the O^{7+} to O^{6+} charge state density ratio ($n(O^{7+})/n(O^{6+})$) and the Fe/O abundance ratio (n(Fe)/n(O)), we develop two compositional thresholds—one for each magnetic polarity—to distinguish coronal hole material from non-coronal hole plasma. We examine the data points that lie below each threshold line and observe an anti-correlation between $n(O^{7+})/n(O^{6+})$ and solar wind speed for both CH-A and CH-B. Thus, we conclude that both of these coronal holes have a CHBL. We also briefly examine the FIP effect in the CHBL for CH-A and CH-B and discuss the properties of the core region in each coronal hole. Finally, we discuss our results in the context of year-to-year solar wind compositional trend and indicate why our techniques for identifying CHBL regions, if applied to other years, need to be adapted.

2. Instrumentation and Dataset

In this study, we use data from the Solar Wind Ion Composition Spectrometer (SWICS), Solar Wind Electron, Proton, and Alpha Monitor (SWEPAM), and Magnetic Field Experiment (MAG) instruments on the ACE spacecraft (Gloeckler et al., 1998, McComas et al., 1998a, Smith et al., 1998). With an electrostatic analyzer (ESA), time-of-flight (TOF) chamber, and solid state detector (SSD), SWICS is capable of measuring a wide range of charge states for a number of heavy elements, including O and Fe, in the energy range of the solar wind (von Steiger et al., 2000, Lepri and Zurbuchen, 2010). The triple-coincidence technique described by Lepri et al. (2001) and Shearer et al. (2014) is extremely effective in eliminating instrumental background and improves measurement accuracy. The SWEPAM instrument produces 3D ion and electron distributions of the solar wind (McComas et al., 1998a), in turn providing plasma parameters such as proton

speed and temperature. We use magnetic field measurements from MAG to determine solar wind polarity via the same method of determining magnetic sector described in Forsyth et al. (1996) and later applied to the ACE measurements in 2003 by Elliott et al. (2010; 2012).

Our study makes use of SWICS 1.1 level 2 data (on a 2-hour averaged time cadence) and 1-hour averaged data from both SWEPAM and MAG, which are publicly available at the ACE science center (http://www.srl.caltech.edu/ACE/ASC/). SWEPAM/MAG data products are aligned with UTC boundaries and have equidistant time stamps, whereas SWICS 1.1 data products are often slightly larger than 2 hours apart and occasionally less than 2 hours apart (see the release notes for SWICS 1.1, SWEPAM, and MAG at http://www.srl.caltech.edu/ACE/ASC/). Our analysis required a dataset with a common set of time stamps for both the SWEPAM/MAG data products and SWICS data products. We accomplished this by taking the values of the desired SWEPAM/MAG data products that fell within each consecutive pair of SWICS time stamps—which we refer to here as a SWICS time interval—and then assigning that average value to a time one hour after the start of the SWICS time interval. The average was assigned to the middle of the SWICS time interval because the time stamp associated with each SWICS 2-hour averaged data point is the beginning of the data collection window for the instrument; thus, the 2-hour average is most representative of the time in the middle of the SWICS time interval (http://www.srl.caltech.edu/ACE/ASC/). When taking the average, we required at least two non-flagged SWEPAM/MAG values; otherwise, the data point was omitted from the dataset. Moreover, we recognized that for SWICS time intervals noticeably greater or less than 2 hours, the actual length of the

collection window was uncertain. For this reason, we also excluded data points that fell within SWICS time intervals which were noticeably longer (fractional year length larger than 0.00024) or shorter (fractional year length smaller than 0.00022) than two hours. We chose these fractional year length criteria because the fractional year equivalent of 2 hours is roughly 0.0002283 for non-leap years. Our time interval length restriction did not remove an appreciable number of points from our dataset; for example, only 4 out of 4325 time intervals in 2003 did not meet our length criteria. Finally, since our study focuses on coronal hole material, we removed any data points associated with ICMEs according to the list of CME start and stop times developed by Richardson and Cane (2004), which can also be found at the ACE science center (http://www.srl.caltech.edu/ACE/ASC/DATA/level3). Similar to Elliott et al. (2012), we remove data points 15 hours before the start and 6 hours after the end of each CME in order to account for uncertainty in the start and stop times.

Our dataset covers all 365 days of the year in 2003 (1/1/2003 to 12/31/2003). We restricted our study to 2003 for three reasons. First, the fast wind streams emitted by CH-A reach some of the highest non-ICME speeds in the ACE dataset (Elliott et al., 2010; Elliott et al., 2012). Since streams produced by CH-B are noticeably slower than those of CH-A, this provides an interesting opportunity to compare the boundary regions of a coronal hole producing extremely fast streams and a coronal hole producing moderately fast streams. Second, we use the T-V box from the Elliott et al. (2012) study to verify the accuracy of our composition-based coronal hole identification methods, and this T-V box is defined based on observations from 2003. Third, the average values of $n(O^{7+})/n(O^{6+})$ and n(Fe)/n(O) fluctuate considerably from year-to-year, and so without modification, the

threshold lines we use in this work would not likely be suitable for other years. We discuss this "baseline shift" effect further in Section 5. It should also be noted that 2003 occurred in the middle of the declining phase of solar cycle 23, a period of moderate solar activity (Atac and Ozguc, 2006, Zhao et al., 2009). In our study, we do not directly map our observations back to source regions on the solar surface. However, we use the coronal hole maps shown in Figure 3 and well as the time series plot in Figure 2d to correlate features of our dataset with particular solar structures.

3. Analysis of Composition Data

Although the anti-correlation between $T(O^{7+}/O^{6+})$—which is proportional to $n(O^{7+})/n(O^{6+})$—and solar wind speed (Geiss et al., 1995, McComas et al., 2002) is well-documented, it is difficult to determine the source of a solar wind stream based on its $n(O^{7+})/n(O^{6+})$ values alone. In outlining a six-category scheme for classifying solar wind, Zhao et al. (2017) report that the median value of $n(O^{7+})/n(O^{6+})$ measured by ACE from coronal hole boundaries between 2000 and 2002 was 0.091, while the median speed was 492 km/s. However, these median values do not reflect the large spread of $n(O^{7+})/n(O^{6+})$ values across all speeds and regardless of magnetic polarity, as shown in Figure 4a, 4b, and 4c. Since $n(O^{7+})/n(O^{6+})$ tends to decrease with increasing proton speed throughout the entire distribution, it is challenging to identify a CHBL region without arbitrarily choosing a speed range. And as argued by Zhao et al. (2017), solar wind speed is not a surefire indicator of source since some coronal holes have been observed emitting streams with speeds close to that of slow wind (Bravo and Stewart, 1997). Compositional signatures that are representative of the FIP effect, like the Fe/O abundance ratio

(n(Fe)/n(O)), are also ineffective as a standalone metric of solar wind source. As demonstrated by Figure 4d, 4e, and 4f, n(Fe)/n(O) also has a wide range of values at all speeds. Also of note is the much weaker anticorrelation between n(Fe)/n(O) and proton speed in comparison to the anticorrelation between $n(O^{7+})/n(O^{6+})$ and proton speed.

In order to identify coronal hole-originating plasma in 2003, then, we plotted both solar wind composition signatures against each other and filtered this distribution according to whether or not the data points fell within the T-V box, as shown in Figure 5. We applied this filtering since Elliott et al. (2012) indicate that the large majority of points that lie within the T-V box represents plasma that originated from coronal holes. We found that low $n(O^{7+})/n(O^{6+})$ values in conjunction with low n(Fe)/n(O) values tend to be typical of data points that lie within the T-V box (Figure 5b). By contrast, points outside the T-V box have a wide range of $n(O^{7+})/n(O^{6+})$ and n(Fe)/n(O) values. For this reason, keeping in mind the differences between the inward-polarity and outward-polarity data in Figures 2 and 4, we chose to isolate coronal hole-originating plasma in our dataset using two different composition threshold lines, one for each polarity.

Figure 6 shows binned $n(O^{7+})/n(O^{6+})$ vs. n(Fe)/n(O) distributions filtered by magnetic polarity. Neither plot seems to indicate an obvious place to draw a threshold line, but the fact that the two distributions have noticeably different shapes suggests the need for two separate compositional threshold lines. To create these threshold lines, we performed a linear fit in log-log space to each of these distributions and collapsed them into one-dimensional distributions along the fit line. Figure 7a and 7b show these fit lines in relation to scatterplots of the outward-polarity and inward-polarity $n(O^{7+})/n(O^{6+})$ vs. n(Fe)/n(O) distributions. Although both fits have a large chi squared value, which is a

result of the sizable variability of solar wind composition, they still provide a mathematical standard by which to collapse each two-dimensional distribution into a one-dimensional distribution. In each instance, we divided the fit line into 100 equidistant intervals and then drew boundaries in between each of these intervals that were perpendicular (in log-log space) to the fit line. Finally, we summed the number of points that fell in between each adjacent pair of boundaries, thus creating a one-dimensional distribution with 100 bins; the result is shown by the black lines in Figure 8a and 8b. We also summed the number of points in each bin with speeds greater than 500 km/s (red line) and the number of points with speeds less than 500 km/s (blue line).

We defined "high-speed" points as having speeds greater than 500 km/s for two reasons. First, although some recent studies (Stakhiv et al., 2015, Zhao et al., 2017) advocate for a categorization of solar wind regimes beyond the fast wind/slow wind dichotomy, 500 km/s is generally accepted as a reasonable threshold for distinguishing fast wind (e.g. Higginson et al., 2017). Furthermore, in describing what they call the boundary wind, a regime which may exist between fast and slow wind, Stakhiv et al. (2015) still recognize compositional differences that occur at 500 km/s. Second, the inward-polarity streams do not reach the extremely fast speeds of the outward-polarity streams, and so a distinction between fast/slow wind at 570 km/s like the T-V box would exclude a large portion of the fast wind with inward polarity. Interestingly, for both polarities in Figures 8a and 8b, the high-speed and the low-speed populations are distinct and have Gaussian-like profiles that overlap. As a result, we chose to draw the composition threshold lines at the intersection of these profiles, represented by a vertical yellow line in Figures 8a and 8b. The composition threshold lines are plotted on top of

the fit lines and scatterplot $n(O^{7+})/n(O^{6+})$ vs. n(Fe)/n(O) distributions in Figures 8c and 8d, and the equations in the form of a power law are also shown.

Following Elliott et al. (2012)'s findings about the outward-polarity and inward-polarity populations that lie within the T-V box, we make the assumption that the overall trends of the data points below each threshold line are representative of CH-A (outward-polarity data) and CH-B (inward polarity data). As shown in Table 1, 97.7% (88.5%) of the points with outward (inward) polarity that lie inside the T-V box also fall below our outward-polarity (inward-polarity) threshold line. Furthermore, Figure 1 indicates that the majority of the high-speed, outward-polarity streams whose data points lie inside the T-V box come from CH-A and the majority of high-speed, inward-polarity streams whose data points lie inside the T-V box come from CH-B. Thus, while we do not presume that all data below each threshold line belongs to CH-A and CH-B, we believe our assumption is a valid one.

Figures 9 and 10 show a typical high-speed stream with outward polarity that occurred between day 232 and day 236 of 2003. All data points displayed lie below our outward-polarity threshold line. In general, $n(O^{7+})/n(O^{6+})$ decreases steadily along the rising edge of the peak (points marked with circles), stays relatively constant near the apex (points marked with triangles), and falls steadily along the declining edge of the peak (points marked with squares). The rising and falling edges, where there is a clear anticorrelation between $n(O^{7+})/n(O^{6+})$ and solar wind speed, are the CHBL, while the flatter apex region is the core of the coronal hole. In all regions of this stream, however, n(Fe)/n(O) values have no strong correlation with solar wind speed. We observed similar trends when looking at all points below each of the threshold lines, as shown in Figure

11. For each $n(O^{7+})/n(O^{6+})$ vs. n(Fe)/n(O) distribution, the points with highest speeds have the lowest $n(O^{7+})/n(O^{6+})$ values, and points with moderate speeds have intermediate $n(O^{7+})/n(O^{6+})$ values. Thus, below each threshold line, there is a noticeable anticorrelation between $n(O^{7+})/n(O^{6+})$ and solar wind speed. Since charge states are frozen-in in the corona (von Steiger et al., 1992), this solar wind structure indicates that both CH-A and CH-B have a CHBL.

4. Discussion

An interesting point of comparison for the high-speed stream from CH-A shown in Figures 9 and 10 is the event depicted in Figure 12 of Foullon et al. (2011), which also involves plasma emitted by a low-latitude coronal hole. Both coronal hole-originating streams show evidence of distinct CHBL and core regions: a monotonic, inverse relationship between $n(O^{7+})/n(O^{6+})$ and proton speed in the CHBL and a nearly flat relationship between these two quantities at the highest speeds. However, there is a striking difference between these two streams in structure relative to speed. For the stream from CH-A, $n(O^{7+})/n(O^{6+})$ starts to flatten at around 690 km/s on the rising edge of the peak and remains relatively flat in the 700-770 km/s range, with some variation in the high-speed portion of the declining edge. By contrast, the flattening of $n(O^{7+})/n(O^{6+})$ for the Foullon et al. (2011) stream occurs at about 520 km/s and persists for a much larger speed range, between 520 and 700 km/s. Since we did not trace our measurements directly back to the Sun, we cannot say for certain what part of CH-A was being observed by ACE from day 232 to day 236 of 2003. It could be that this particular stream came from a place close to the edge of the coronal hole such that ACE observed only a small

part of the core region; this would explain why the flattening of $n(O^{7+})/n(O^{6+})$ vs. proton speed occurs for a small range of speeds. In Figure 11a, the highest speeds from CH-A reach about 860 km/s, nearly 100 km/s greater than the maximum speed reached by the peak in Figures 9 and 10. Moreover, among points with $n(O^{7+})/n(O^{6+})$ values of 0.04 or less, the distribution in Figure 11a is fairly homogeneous in terms of color (representative of the mean proton speed of each bin). Conversely, among points with $n(O^{7+})/n(O^{6+})$ values of 0.04 or greater but still below the outward-polarity threshold line, there is a consistent gradient in average speed. Thus, it is likely that the core region of CH-A has a speed range 700 to 860 km/s, the breadth of which (160 km/s) is similar to that of the Foullon et al. (2011) stream. Regardless of the size of the core region, however, the CHBL for CH-A is much thicker than the CHBL measured by Foullon et al. (2011).

As for CH-B, there is a clear gradient in color moving perpendicularly from the inward-polarity threshold line toward lower $n(O^{7+})/n(O^{6+})$ and n(Fe)/n(O) values in Figure 11b, although the core region has much lower speeds (around 700 km/s, indicated by the color yellow) than CH-A's core region. Accordingly, both the core region and the CHBL for CH-B have smaller speed ranges than the corresponding structures of CH-A. This may indicate that the size of a CHBL region depends on the overall size of the coronal hole, but more measurements of CHBL thickness beyond the two coronal holes studied here are needed to validate this claim. Schwadron et al. (2005) suggest that the CHBL has an intrinsic width that is dependent on the escape time of coronal plasma and the motion of field lines across the coronal hole boundary; perhaps analysis of Parker Solar Probe and/or Solar Orbiter data can provide some insight into the size of the CHBL relative to its associated coronal hole. Another major difference between CH-A and CH-

B is the nature of the FIP effect in each hole. For CH-A, there is a large spread of n(Fe)/n(O) values at all speeds, and while there may be a slight tendency for lower n(Fe)/n(O) values in the core relative to the CHBL, the difference is very small. On the other hand, while there is still a decently large spread of n(Fe)/n(O) values in all parts of the distribution below the inward-polarity threshold line, n(Fe)/n(O) values in the core region of CH-B are clearly lower on average than those of the CHBL. It is unclear why this is the case, as previous studies (e.g. von Steiger and Zurbuchen, 2016) have shown that the FIP is much more pronounced in slow wind than fast wind. The evolution of CHBL material as it propagates through interplanetary space may play a role, as Foullon et al. (2011) describe a means by which a high speed stream (i.e. from the core region of a coronal hole) can interact with a CHBL stream and affect its composition. Since we only used measurements from 1 AU in our study, we cannot make any determinations about how the CHBL and core streams evolved as they propagated. To this end, observations closer to the Sun, such as data from Solar Orbiter, are likely to be useful in further studies.

Although we are confident in our methods to match ACE observations with the global coronal hole maps in Figure 3, we recognize that one of the limitations of our study is the fact that we do not directly trace measurements back to the Sun along solar field lines. For an example of a study which does employ tracing techniques, see Zhao et al. (2017), which uses SOHO and STEREO images in conjunction with a Potential Field Solar Source model. Other heliospheric models that may be useful for CHBL analysis are found at the Community Coordinated Modeling Center (https://ccmc.gsfc.nasa.gov/). We also emphasize that our compositional thresholds are specific to 2003 and should be

adapted before being used to evaluate data from other years. Previous studies (e.g. Lepri et al., 2013, Zhao et al., 2017) have shown that solar wind composition is dependent on the phase of the solar cycle. As an example, Figure 12 shows the mean $n(O^{7+})/n(O^{6+})$ value at different solar wind speed ranges for the years 2002, 2003, and 2009. The average value curves for 2002 and 2003 (near solar maximum) are similar, while the curve for 2009 (closer to solar minimum) is markedly different, indicating a significant baseline shift of $n(O^{7+})/n(O^{6+})$ values. Additionally, 2009 had no fast wind streams with speeds greater than 700 km/s. The implication of these major differences is that a fixed threshold line based on $n(O^{7+})/n(O^{6+})$ or other compositional measurements should not be used to distinguish coronal hole material from non-coronal hole material for a large time range. Instead, should our threshold line method be adapted for a different year, such analysis should be based on a fit line to the $n(O^{7+})/n(O^{6+})$ vs. n(Fe)/n(O) distribution for that year.

5. Conclusions

In this study, we used ACE composition data to identify a distinct CHBL and core region in two prominent coronal holes of 2003, which we refer to as CH-A and CH-B. Specifically, in each of the two coronal holes, we observed a clear anticorrelation between $n(O^{7+})/n(O^{6+})$ and solar wind speed which levels off at the highest speeds. In the larger coronal hole, CH-A, we observed a CHBL with a broad speed range and no change in the FIP effect (based on measurements of n(Fe)/n(O) values) from the CHBL to the core region. In CH-B, the CHBL had a smaller speed range than that of CH-A, but had higher n(Fe)/n(O) values than the core region. From these findings, we conclude that both

large and small equatorial holes can have CHBL structure. Compositional analysis techniques like the ones we employed in this work to examine high-speed streams can be exploited in future studies of coronal holes and fast wind. Topics worthy of further research, including the FIP effect in coronal hole material and the evolution of CHBL-originating streams in interplanetary space, may benefit greatly from compositional analysis.

6. Acknowledgements

The authors would like to thank the ACE team, and in particular the SWICS, SWEPAM, and MAG instrument teams, for making their data and release notes publically available (the SWICS, SWEPAM, and MAG Level 2 data can be found at the ACE science center website, http://www.srl.caltech.edu/ACE/ASC/). The authors acknowledge using NASA/GSFC's CDAWeb to obtain these data products. This research at the University of Texas at San Antonio and the Southwest Research Institute was supported by NASA-HGI NNX17AI94G and NASA contract NNG04EB99C. H. A. Elliott and S. T. Lepri are supported by NASA-HGI NNX17AI94G, and S. A. Fuselier is supported by NASA contract NNG04EB99C.

Figures and Captions

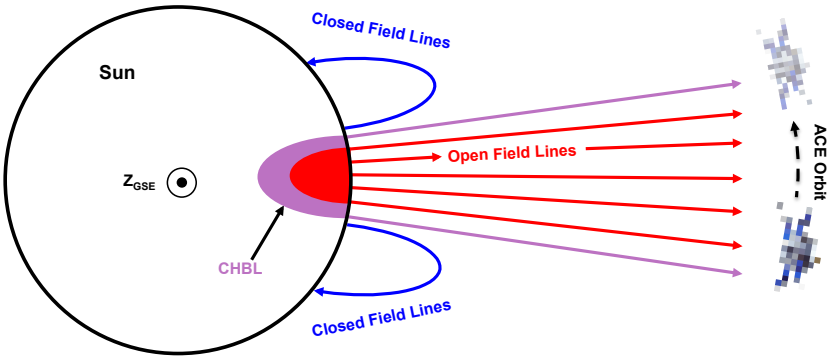

Figure 1: Cartoon of the Sun in the GSE X-Y plane showing a low-latitude coronal hole with a CHBL, solar magnetic field lines, and the ACE spacecraft; distances are not to scale. Closed field lines are blue, open field lines that correspond to the coronal hole core are red, and open field lines that correspond to the CHBL are lavender. It should be noted that coronal holes are features of the corona, not the surface of the Sun, which is not explicitly shown in this cartoon. For a more detailed depiction of a CHBL signature from a low-latitude coronal hole detected by STEREO, as well as the propagation of solar field lines including the effects of the Parker spiral, see Figure 10 of Foullon et al. (2011). Another helpful depiction of CHBL structure is Figure 4 of McComas et al. (2002).

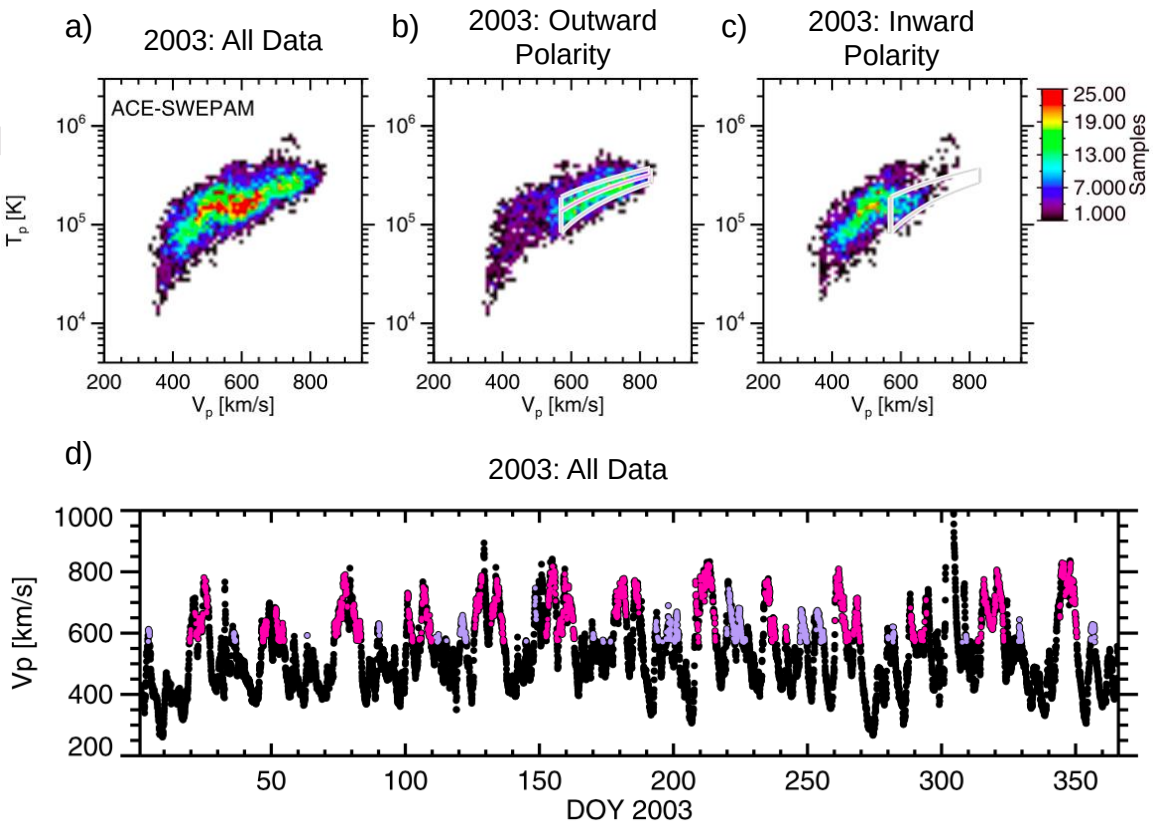

Figure 2: (a) Distribution of solar wind proton temperature (T) versus proton speed (V) for all of 2003. In this panel, as well as panels (b) and (c), the color represents the number of data points in each bin. **(b)** 2003 T-V distribution for outward polarity only, with a box highlighting a high-speed population corresponding to coronal hole material. The pink line is a linear fit to the data points with outward polarity plotted between V = 570 km/s and V = 830 km/s. The upper (lower) boundary of the T-V box has an intercept 1.2 (0.8) times that of the pink fit line, and the left and right boundaries of the box are at 570 km/s and 830 km/s, respectively. **(c)** 2003 T-V distribution for inward polarity only with the T-V box from panel (b) overplotted. **(d)** Proton speed versus time in 2003. Pink data points lie within the T-V box and have outward polarity, lavender points lie within the T-V box and have inward polarity, and black points lie outside of the T-V box or are associated with an ICME. This figure is an adaptation of plots that were originally published in Elliott et al. (2012).

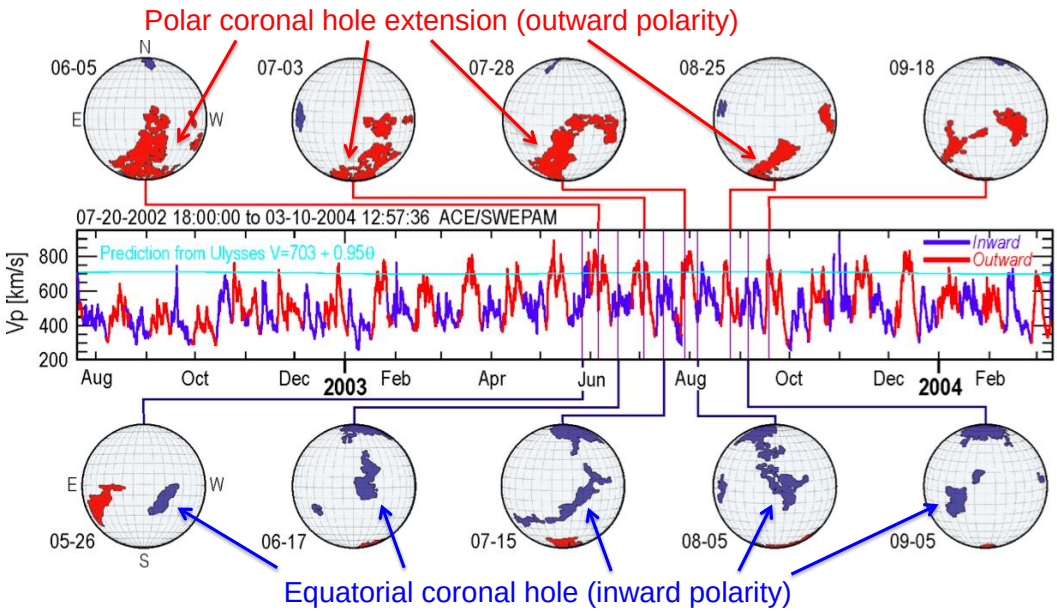

Figure 3: Proton speed (which is indicative of solar wind speed) and magnetic polarity versus time between early 2002 and late 2004 along with coronal hole maps of the Sun for selected dates. Inward polarity is colored blue, while outward polarity is colored red. There was a large coronal hole extension from the southern pole with outward polarity that lasted for most of the year, shown in the top row of maps. The maps on the bottom row show the evolution of a smaller coronal hole with inward polarity near the equator. This figure is an adaptation of a plot originally published in Elliott et al. (2010) and also used in Elliott et al. (2012).

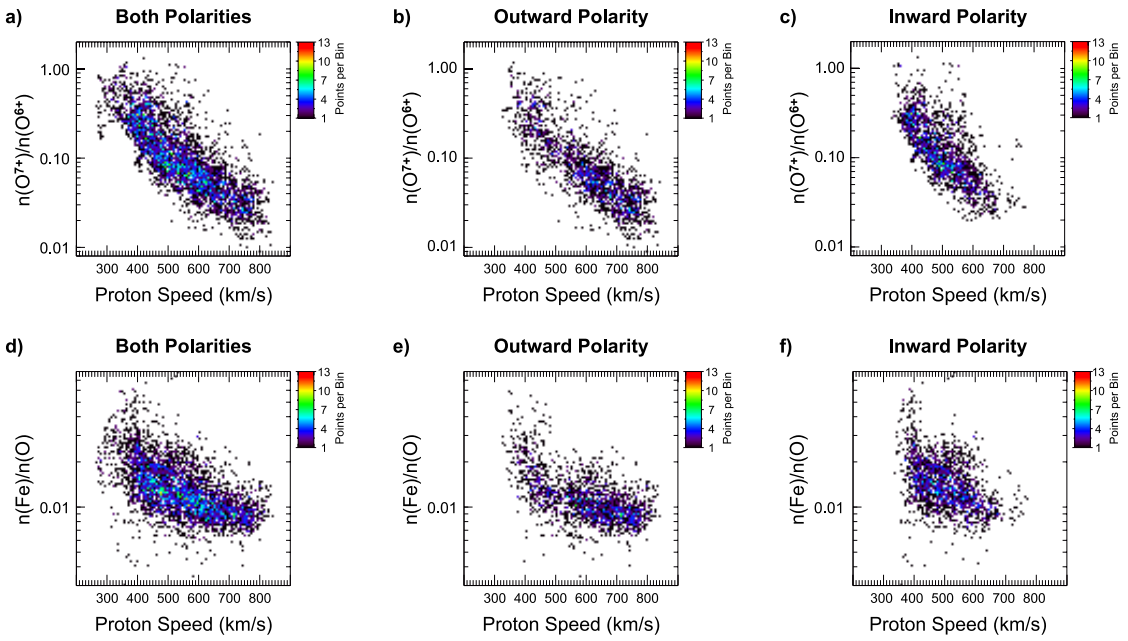

Figure 4: Binned distributions of $n(O^{7+})/n(O^{6+})$ versus solar wind proton speed—panels (a), (b), and (c)—and n(Fe)/n(O) versus solar wind proton speed—panels (d), (e), and (f)—for 2003. Panels (a) and (d) have no filtering by magnetic polarity, panels (b) and (e) show only data points with outward polarity, and panels (c) and (f) show only data points with inward polarity. The unfiltered distributions contain some data points with no defined magnetic polarity. As with all binned distribution plots in this paper, the vertical and horizontal axes each have 100 bins. Here, the color corresponds to the number of points per bin. Regardless of magnetic polarity, $n(O^{7+})/n(O^{6+})$ has a strong anticorrelation with proton speed, while n(Fe)/n(O) tends to decrease slightly with increasing proton speed.

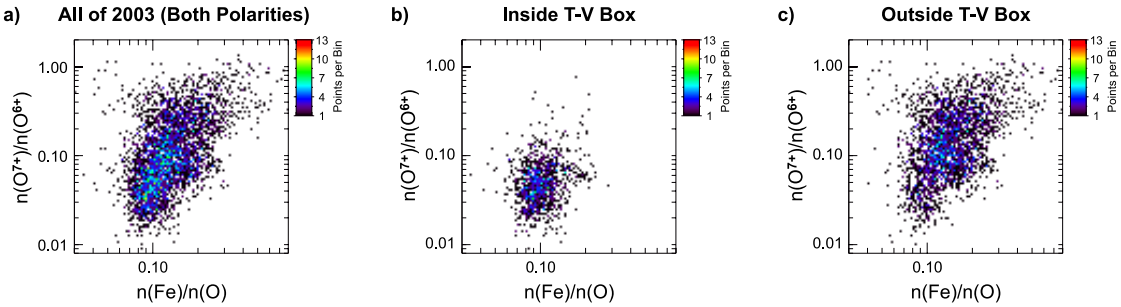

Figure 5: (a) Binned distribution of $n(O^{7+})/n(O^{6+})$ versus n(Fe)/n(O) for all of 2003. No filtering based on polarity has been applied. **(b)** Binned $n(O^{7+})/n(O^{6+})$ vs. n(Fe)/n(O) distribution of the points that lie within the T-V box defined by Elliott et al. (2012). The majority of points are concentrated in the lower left part of the distribution, typically having both low $n(O^{7+})/n(O^{6+})$ and low n(Fe)/n(O) values. **(c)** Binned $n(O^{7+})/n(O^{6+})$ vs. n(Fe)/n(O) distribution of the points that lie outside the T-V box. The points outside the T-V box do not appear to exhibit a particular trend.

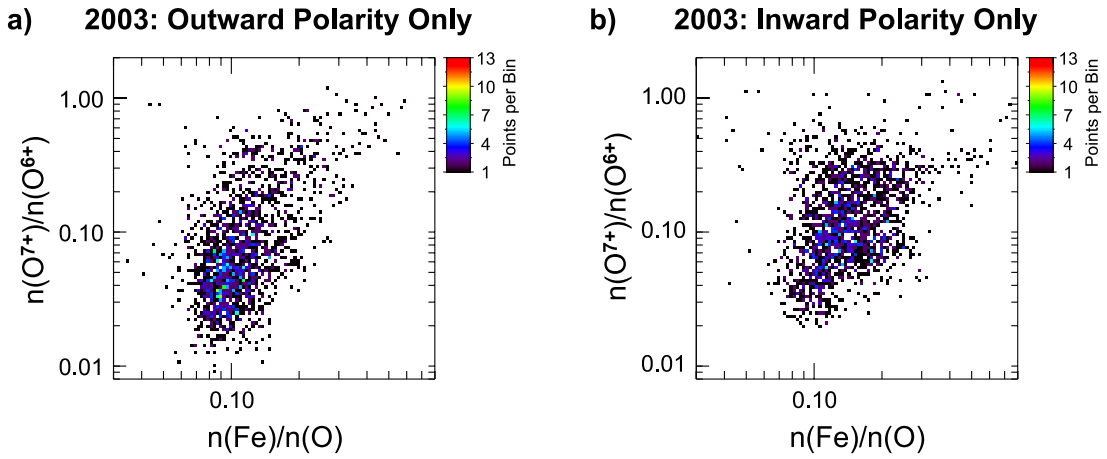

Figure 6: (a) Binned $n(O^{7+})/n(O^{6+})$ versus n(Fe)/n(O) distribution of the points that have outward polarity in 2003. **(b)** Binned $n(O^{7+})/n(O^{6+})$ versus n(Fe)/n(O) distribution of the points that have inward polarity for 2003.

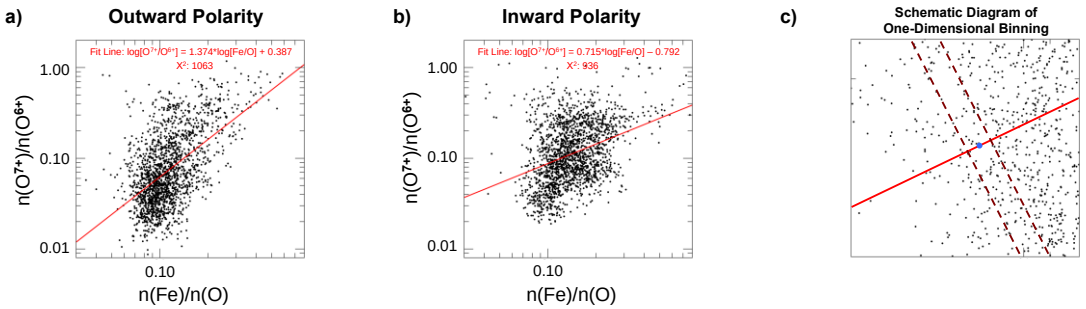

Figure 7: (a) Scatterplot $n(O^{7+})/n(O^{6+})$ versus n(Fe)/n(O) distribution for outward polarity only with a fit line overplotted in red. This fit line, as well as the fit line in panel (b), are linear fits to $\log[n(O^{7+})/n(O^{6+})]$ and log[n(Fe)/n(O)]. **(b)** Scatterplot $n(O^{7+})/n(O^{6+})$ vs. n(Fe)/n(O) distribution for inward polarity only, also with a fit line overplotted in red. **(c)** A visual representation of one of the bins used to create the one-dimensional distribution for the outward-polarity data shown in Figure 8. The points within the bin boundaries are collapsed to the center of the bin along the fit line, shown as a blue dot. The fit line appears in red, while the bin boundaries are maroon. The distribution of points shown in this panel is not actual data and is not necessarily to scale.

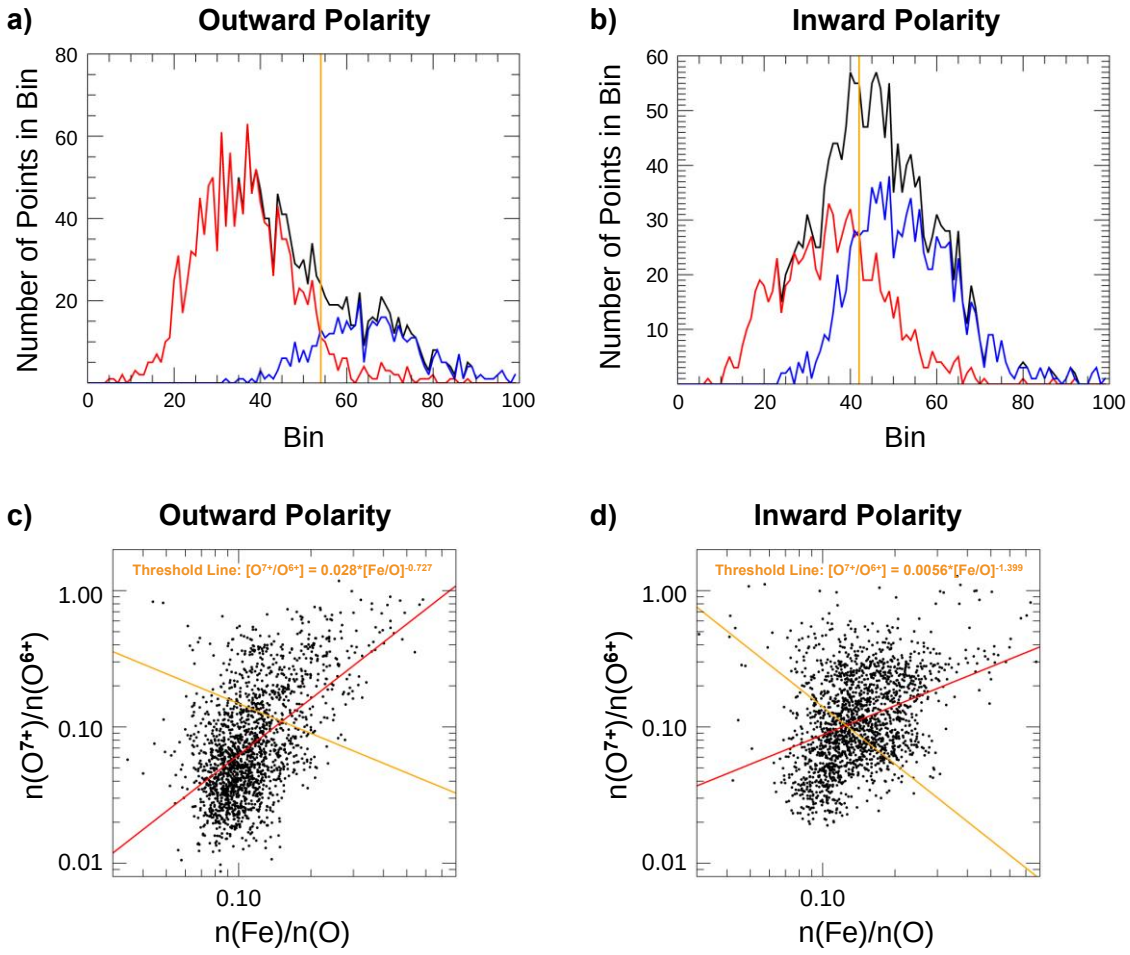

Figure 8: (a) A one-dimensional distribution of the points in Figure 7a collapsed along the fit line. There are 100 bins in this distribution. The red line represents points in each bin with speeds greater than 500 km/s, the blue line represents points in each bin with speeds less than 500 km/s, and the black line represents the sum of all points. The vertical yellow line at bin 54 marks the intersection of the high-speed and low-speed populations. **(b)** One-dimensional distribution of points in Figure 7b using the same method. Here, the intersection of high-speed and low-speed populations is at bin 42. **(c) and (d)** Scatterplot $n(O^{7+})/n(O^{6+})$ vs. n(Fe)/n(O) distributions for each polarity with their respective fit lines (in red) and threshold lines (in yellow) overplotted. The threshold lines are perpendicular to the fit lines, but do not appear as such in these plots since the x- and y-axes have different scales. The equations for the threshold lines are given in power law form.

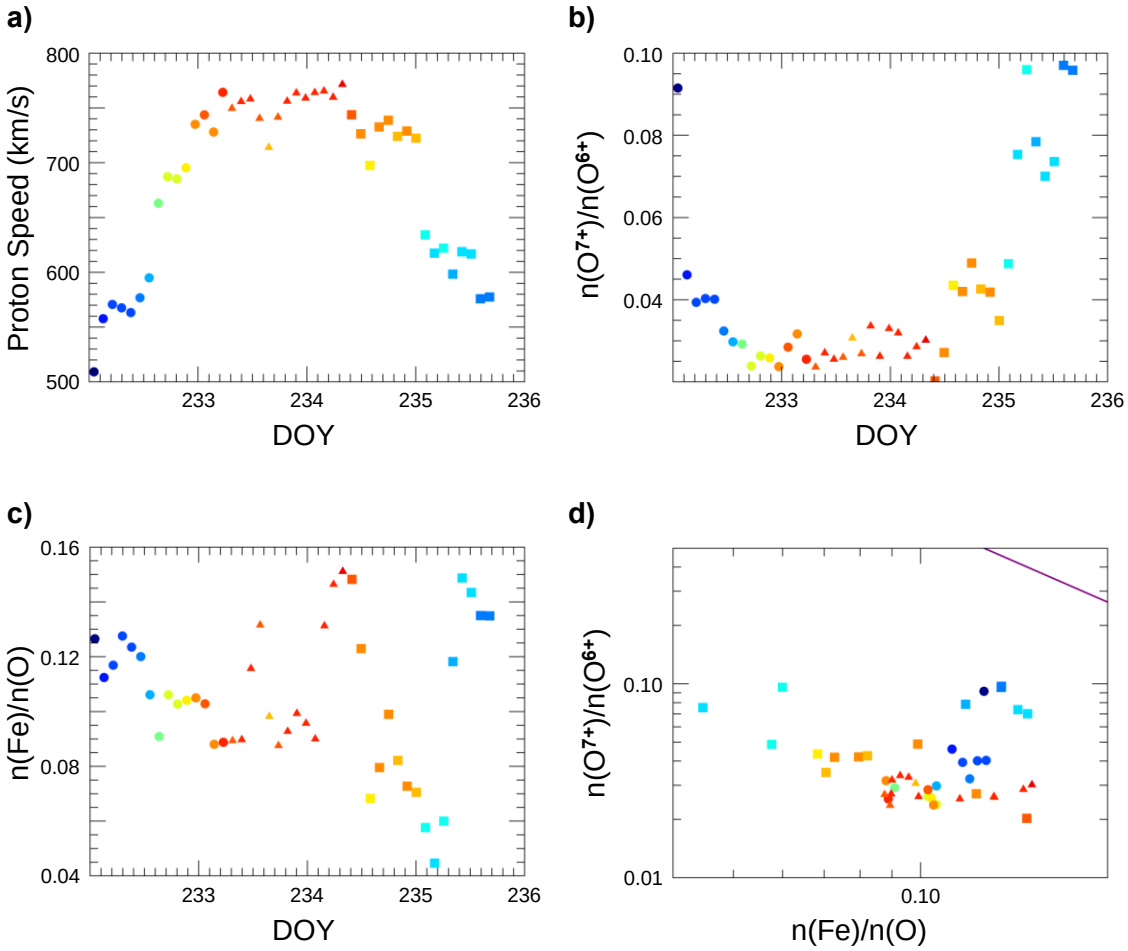

Figure 9: (a) A typical high-speed peak during 2003; this particular stream has outward polarity. The color is indicative of solar wind speed, with blue representing slower speeds and red representing faster speeds. Points marked by circles are part of the rising phase, points marked with squares are part of the declining phase, and points marked by triangles are points near the apex of the peak which are not definitively part of the rising or declining phases. **(b)** $n(O^{7+})/n(O^{6+})$ versus DOY for the peak shown in panel (a). $n(O^{7+})/n(O^{6+})$ is plotted with a linear scale in order to accentuate the difference between the sloping sides and apex of the peak. **(c)** $n(O^{7+})/n(O^{6+})$ versus DOY for the peak shown in panel (a). **(d)** A scatterplot $n(O^{7+})/n(O^{6+})$ versus n(Fe)/n(O) distribution (with logarithmic axes) of the same peak shown in panel (a); the outward-polarity threshold line is shown in purple for reference. The color-coding and symbols are the same for all panels.

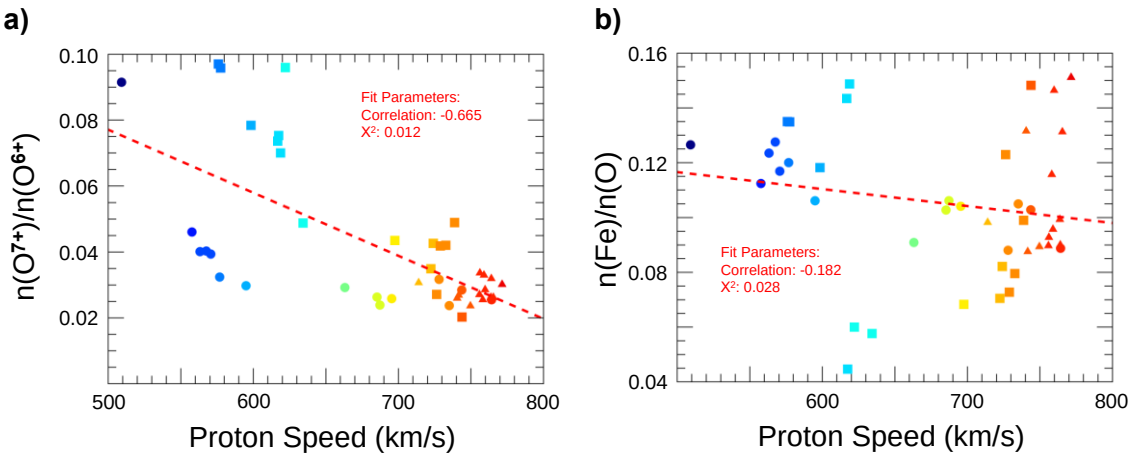

Figure 10: (a) $n(O^{7+})/n(O^{6+})$ versus proton speed for the peak shown in Figure 9a. There is a clear anticorrelation between these two quantities. **(b)** n(Fe)/n(O) versus proton speed for the peak shown in Figure 9a. These two quantities do not have a strong correlation.

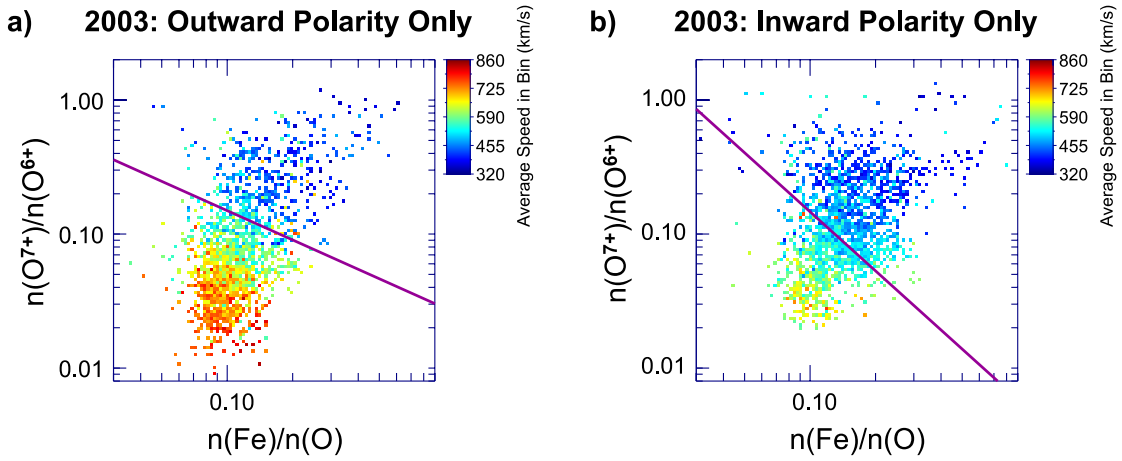

Figure 11: (a) Binned $n(O^{7+})/n(O^{6+})$ versus n(Fe)/n(O) distribution for outward polarity only, with the color representing the mean proton speed of the points that lie within each bin. The outward-polarity threshold line is overplotted in purple. **(b)** Binned $n(O^{7+})/n(O^{6+})$ versus n(Fe)/n(O) distribution for inward polarity with the inward-polarity threshold line overplotted in purple.

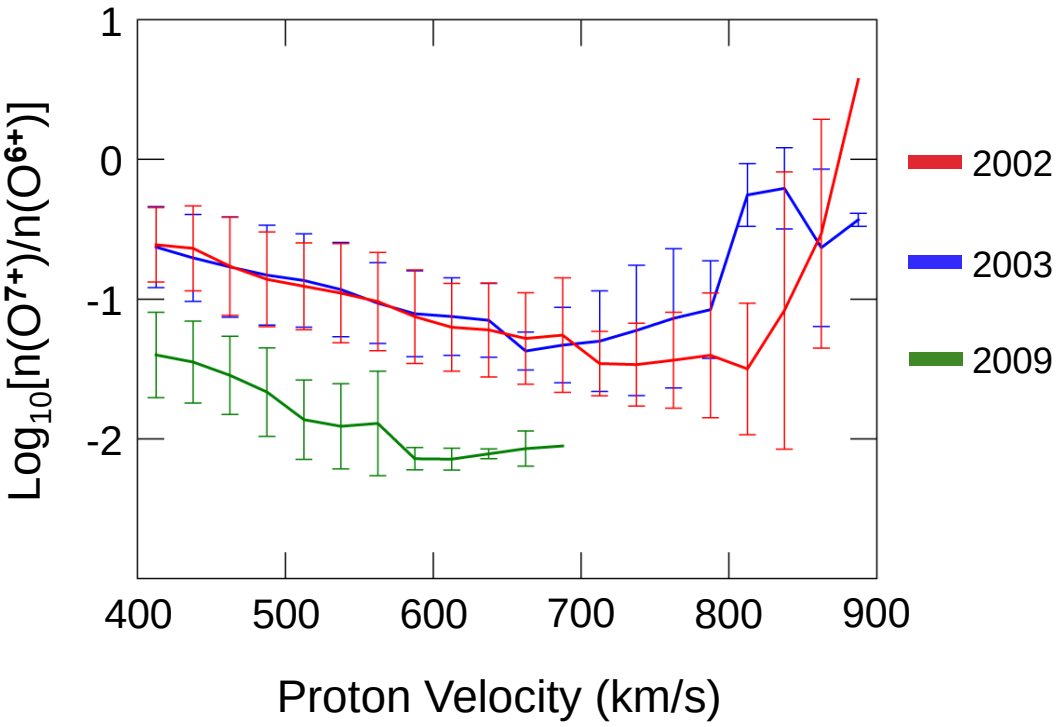

Figure 12: The mean value of $n(O^{7+})/n(O^{6+})$ at each 25 km/s interval between 400 km/s and 900 km/s for 2002 (blue curve), 2003 (red curve), and 2009 (green curve). The errorbars represent the standard deviation in logarithmic space. The maximum solar wind speed measured by ACE in 2009 was about 676 km/s, so the green curve is truncated compared to the other curves. Regardless, the profile of average $n(O^{7+})/n(O^{6+})$ values for 2009 is shifted significantly compared to those of 2002 and 2003. Many such shifts in average values have occurred over the course of the ACE mission.

	Inward polarity	Outward polarity
Total number of points	1829	1822
Number of points below threshold line (percentage of total points)	759 (41.5%)	1362 (74.8%)
Number of points inside T-V box percentage of total points)	287 (15.7%)	838 (46.0%)
Number of points both inside T-V box and below threshold line (percentage of total points inside T-V box)	254 (88.5%)	819 (97.7%)

Table 1: Summary of points in the dataset in relation to our composition threshold lines. We tabulate the number of points in our dataset that lie within and outside of the T-V box and show their relationship to the composition threshold lines. The percentages in the second and third rows are with respect to the total number of points (top row). In the fourth row, the percentages are with respect to the total number of points that lie inside the T-V box (third row). For both polarities, the large majority of points inside the T-V box also lie below the corresponding threshold line.

7. References

Atac, T. and Ozguc, A. (2006). Overview of the solar activity during solar cycle 23, *Solar Physics, 233,* 139-153. https://doi.org/10.1007/s11207-006-1112-3

Bravo, S. and Stewart, G. A. (1997). Fast and slow wind from solar coronal holes, *The Astrophysical Journal, 489,* 992-999. https://doi.org/10.1086/304789

Cranmer, S. R. (2002). Coronal Holes and the High-Speed Solar Wind, *Space Science Reviews, 101,* 229-294. https://doi.org/10.1023/A:1020840004535

Elliott, H. A., Henney, C. J., McComas, D. J., Smith, C. W., and Vasquez, B. J. (2012). Temporal and radial variation of the solar wind temperature-speed relationship, *Journal of Geophysical Research, 117,* A09102, https://doi.org/10.1029/2011JA017125

Elliott, H. A., McComas, D. J., Matthaeus, W. H., and Henney, C. J. (2010). Solar wind speed and temperature relationship, *AIP Conference Proceedings, 1216,* 98-101. https://doi.org/10.1063/1.3395974

Forsyth, R. J., Balogh, A., Smith, E. J., Erdös, G., and McComas, D. J. (1996). The underlying Parker spiral structure in the Ulysses magnetic field observations, 1990-1994, *Journal of Geophysical Research, 101*(A1), 395-403. https://doi.org/10.1029/95JA02977

Foullon, C., Lavraud, B., Luhmann, J. G., Farrugia, C. J., Retino, A., Simunac, K. D. C., et al. (2011). Plasmoid releases in the heliospheric current sheet and associated coronal hole boundary layer evolution, *The Astophysical Journal, 737,* 16-31. https://doi.org/10.1088/0004-637X/737/1/16

Geiss, J., Gloeckler, G., and von Steiger, R. (1995). Origin of the solar wind from composition data, *Space Science Reviews, 72,* 49-60. https://doi.org/10.1007/BF00768753

Gloeckler, G., Cain, J., Ipavich, F. M., Tums, E. O., Bedini, P., Fisk, L. A. et al. (1998). Investigation of the composition of solar and interstellar matter using solar wind and pickup ion measurements with SWICS and SWIMS on the ACE spacecraft, *Space Science Reviews, 86,* 497-539. https://doi.org/10.1023/A:1005036131689

Higginson, A. K., Antiochos, S. K., DeVore, C. R., Wyper, P. F., and Zurbuchen, T. H. (2017). Dynamics of Coronal Hole Boundaries, *The Astrophysical Journal, 837,* 113-130. https://doi.org/10.3847/1538-4357/837/2/113

Hollweg, J. V. and Isenberg, P. A. (2002). Generation of the fast solar wind: a review with emphasis on the resonant cyclotron interaction, *Journal of Geophysical Research, 107*(A9), 1147-1183. https://doi.org/10.1029/2001JA000270

Hundhausen, A. J. (1977). An interplanetary view of coronal holes, in *Coronal Holes and High Speed Wind Streams*, edited by J. B. Zirker, p. 225, Colorado Associated University Press, Boulder

Krista, L. D., McIntosh, S. W., and Leamon, R. J. (2018). The Longitudinal Evolution of Equatorial Coronal Holes, *The Astrophysical Journal, 155*(4), 153. https://doi.org/10.3847/1538-3881/aaaebf

Laming, J. M. (2015). The FIP and Inverse FIP Effects in Solar and Stellar Coronae, *Living Reviews in Solar Physics, 12*, 2. https://doi.org/10.1007/lrsp-2015-2

Laming, J. M., and Lepri, S. T. (2007). Ion Charge States in the Fast Solar Wind: New Data Analysis and Theoretical Refinements, *The Astrophysical Journal, 660*(2), 1642-1652. https://doi.org/10.1086/513505

Landi, E. (2008). The off-disk thermal structure of a polar coronal hole, *The Astrophysical Journal, 685*(2), 1270-1276. https://doi.org/10.1086/591225

Lepri, S. T., Landi, E., and Zurbuchen, T. H. (2013). Solar wind heavy ions over solar cycle 23: *ACE*/SWICS measurements, *The Astrophysical Journal, 768*, 94-106. https://doi.org/10.1088/0004-637X/768/1/94

Lepri, S. T. and Zurbuchen, T. H. (2010). Direct observational evidence of filament material within interplanetary coronal mass ejections, *The Astrophysical Journal Letters, 723*, L22-L27. https://doi.org/10.1088/2041-8205/723/1/L22

Lepri, S. T., Zurbuchen, T. H., Fisk, L. A., Richardson, I. G., Cane, H. V., and Gloeckler, G. (2001). Iron charge distribution as an identifier of interplanetary coronal mass ejections, *Journal of Geophysical Research, 106*(A12), 29231-29238. https://doi.org/10.1029/2001JA000014

McComas, D. J., Bame, S. J., Barker, P., Feldman, W. C., Phillips, J. L., Riley, P., and Griffee, J. W. (1998a). Solar Wind Electron Proton Alpha Monitor (SWEPAM) for the Advanced Composition Explorer, *Space Science Reviews, 86*, 563-612. https://doi.org/10.1023/A:1005040232597

McComas, D. J., Riley, P., Gosling, J. T., Balogh, A., and Forsyth, R. (1998b). Ulysses' rapid crossing of the polar coronal hole boundary, *Journal of Geophysical Research, 103*(A2), 1955-1967. https://doi.org/10.1029/97JA01459

McComas, D. J., Elliott, H. A., Schwadron, N. A., Gosling, J. T., Skoug, R. M., and Goldstein, B. E. (2003). The three-dimensional solar wind around solar maximum, *Geophysical Research Letters, 30*(10), 1517-1520. https://doi.org/10.1029/2003GL017136

McComas, D. J., Elliott, H. A., and von Steiger, R. (2002). Solar wind from high-latitude coronal holes at solar maximum, *Geophysical Research Letters, 29*(9), 1314-1317. https://doi.org/10.1029/2001GL013940

Meyer, J.-P. (1985). The baseline composition of solar energetic particles, *The Astrophysical Journal Supplement Series, 57,* 151-171. https://doi.org/10.1086/191000

Owocki, S. P., Holzer, T. E., and Hundhausen, A. J. (1983). The solar wind ionization state as a coronal temperature diagnostic, *The Astrophysical Journal, 275,* 354-366. https://doi.org/10.1086/161538

Richardson, I. G., and Cane, H. V. (2004). Identification of interplanetary coronal mass ejections at 1 AU using multiple solar wind plasma composition anomalies, *Journal of Geophysical Research, 109,* A09104. https://doi.org/10.1029/2004JA010598

Schwadron, N. A., McComas, D. J., Elliott, H. A., Gloeckler, G., Geiss, J., and von Steiger, R. (2005). Solar wind from the coronal hole boundaries, *Journal of Geophysical Research, 110,* A04104. https://doi.org/10.1029/2004JA010896

Shearer, P., von Steiger, R., Raines, J. M., Lepri, S. T., Thomas, J. W., Gilbert, J. A., Landi, E., and Zurbuchen, T. H. (2014). The solar wind neon abundance observed with ACE/SWICS and ULYSSES/SWICS, *The Astrophysical Journal, 789*, 60-69. https://doi.org/10.1088/0004-637X/789/1/60

Smith, C. W., L'Heureux, J., Ness, N. F., Acuña, M. H., Burlaga, L. F., and Scheifele, J. (1998). The ACE Magnetic Fields Experiment, *Space Science Reviews, 86,* 613-632. https://doi.org/10.1023/A:1005092216668

Stakhiv, M., Landi, E., Lepri, S. T., Oran, R., and Zurbuchen, T. H. (2015). On the origin of mid-latitude fast wind: challenging the two-state solar wind paradigm, *The Astrophysical Journal, 801*(2), 100-107. https://doi.org/10.1088/0004-637X/801/2/100

Stakhiv, M., Lepri, S., Landi, E., Tracy, P., and Zurbuchen, T. H. (2016). On solar wind origin and acceleration: Measurements from ACE, *The Astrophysical Journal, 829,* 117-130. https://doi.org/10.3847/0004-637X/829/2/117

von Steiger, R., Christon, S. P., Gloeckler, G., and Ipavich, F. M. (1992). Variable Carbon and Oxygen Abundances in the Solar Wind as Observed in Earth's Magnetosheath by AMPTE/CCE, *The Astrophysical Journal, 389,* 791. https://doi.org/10.1086/171252

von Steiger, R., Schwadron, N. A., Fisk, L. A., Geiss, J., Gloeckler, G., Hefti, S. et al.

(2000). Composition of quasi-stationary solar wind flows from Ulysses/Solar Wind Ion Composition Spectrometer, *Journal of Geophysical Research, 105*(A12), 27217-27238. https://doi.org/10.1029/1999JA000358

von Steiger, R., and Zurbuchen, T. H. (2016). Solar metallicity derived from in situ solar wind composition, *The Astrophysical Journal, 816,* 13-20. https://doi.org/10.3847/0004-637X/816/1/13

Zhao, L., Landi, E., Lepri, S. T., Gilbert, J. A., Zurbuchen, T. H., Fisk, L. A., and Raines, J. M. (2017). On the Relation between the In Situ Properties and the Coronal Sources of the Solar Wind, *The Astrophysical Journal, 846,* 135-145. https://doi.org/10.3847/1538-4357/aa850c

Zhao, L., Zurbuchen, T. H., and Fisk, L. A. (2009). Global distribution of the solar wind during solar cycle 23: ACE observations, *Geophysical Research Letters, 36,* L14104. https://doi.org/10.1029/2009GL039181

Zirker, J. B. (1977). Coronal Holes and High-Speed Wind Streams, *Reviews of Geophysics and Space Physics, 15*(3), 257-269. https://doi.org/10.1029/RG015i003p00257

Zurbuchen, T. H. (2007). A new view of the coupling of the Sun and the heliosphere, *Annual Review of Astronomy and Astrophysics, 45*(1), 297-338. https://doi.org/10.1146/annurev.astro.45.010807.154030